

# A possible long-term and very-deep aseismic slip event activating seismicity off Tohoku

Fumiaki Tomita<sup>1</sup>

<sup>1</sup>IRIDeS, Tohoku University

June 23, 2023

## Abstract

Various slips at plate interfaces in subduction zones have been documented, and the role of aseismic slips in strain release and stress re-distribution has been revealed. Prior to the M9 2011 Tohoku earthquake in Japan, various small-scale aseismic slip events which possibly affected the occurrence of the 2011 Tohoku earthquake had been reported. However, the small-scale aseismic slip behaviors after the M9 2011 Tohoku earthquake have not been well-clarified because the dominant postseismic deformation of the 2011 Tohoku earthquake has hidden minor aseismic slips. In this study, we performed trajectory models for the GNSS time-series after eliminating the postseismic deformation of the 2011 Tohoku earthquake, and we extracted afterslips followed by M7 class earthquakes, and an ongoing long-term aseismic slip event (L-ASE) since late 2019. The spatial extent of these aseismic slips was also clarified, and the 2019 L-ASE was estimated to be in the down-dip area of the seismogenic zone. As a similar L-ASE was also found before the 2011 Tohoku earthquake, a comparison of these L-ASEs suggests that the repeated L-ASEs promoted strain accumulation in the shallow plate interface, including the M9 rupture area, and may be markers preceding M7 class seismicity. Because L-ASEs are key phenomena in assessing sequential seismic behaviors in the Tohoku subduction zone, monitoring the ongoing L-ASE and investigating its physical interaction with other slip behaviors is important.

## Hosted file

965371\_0\_art\_file\_11060456\_rvtqvp.docx available at <https://authorea.com/users/550642/articles/648065-a-possible-long-term-and-very-deep-aseismic-slip-event-activating-seismicity-off-tohoku>

## Hosted file

965371\_0\_supp\_11060458\_rvtqvp.docx available at <https://authorea.com/users/550642/articles/648065-a-possible-long-term-and-very-deep-aseismic-slip-event-activating-seismicity-off-tohoku>



## PUBLICATIONS

### A possible long-term and very-deep aseismic slip event activating seismicity off Tohoku

F. Tomita<sup>1</sup>

<sup>1</sup>International Research Institute of Disaster Science, Tohoku University, 468-1 Aramaki-Aza-Aoba, Aoba-ku, Sendai, 980-8572, Japan.

Corresponding author: Fumiaki Tomita (fumiaki.tomita.d8@tohoku.ac.jp)

#### Key Points:

- GNSS observations suggest a possible long-term aseismic slip event since late 2019 off Tohoku.
- The long-term aseismic slip event is located at the deep plate interface, which is same or deeper than the similar event since 2002.
- The repeated occurrence of the aseismic slip events may activate seismicity at the shallower plate interface.

## 19 **Abstract**

20 Various slips at plate interfaces in subduction zones have been documented, and the role  
21 of aseismic slips in strain release and stress re-distribution has been revealed. Prior to the M9  
22 2011 Tohoku earthquake in Japan, various small-scale aseismic slip events which possibly  
23 affected the occurrence of the 2011 Tohoku earthquake had been reported. However, the small-  
24 scale aseismic slip behaviors after the M9 2011 Tohoku earthquake have not been well-clarified  
25 because the dominant postseismic deformation of the 2011 Tohoku earthquake has hidden minor  
26 aseismic slips. In this study, we performed trajectory models for the GNSS time-series after  
27 eliminating the postseismic deformation of the 2011 Tohoku earthquake, and we extracted  
28 afterslips followed by M7 class earthquakes, and an ongoing long-term aseismic slip event (L-  
29 ASE) since late 2019. The spatial extent of these aseismic slips was also clarified, and the 2019  
30 L-ASE was estimated to be in the down-dip area of the seismogenic zone. As a similar L-ASE  
31 was also found before the 2011 Tohoku earthquake, a comparison of these L-ASEs suggests that  
32 the repeated L-ASEs promoted strain accumulation in the shallow plate interface, including the  
33 M9 rupture area, and may be markers preceding M7 class seismicity. Because L-ASEs are key  
34 phenomena in assessing sequential seismic behaviors in the Tohoku subduction zone, monitoring  
35 the ongoing L-ASE and investigating its physical interaction with other slip behaviors is  
36 important.

## 37 **Plain Language Summary**

38 Along a plate interface in a subduction zone, we can find various types of slip behaviors,  
39 such as various magnitudes of interplate earthquakes, afterslip, slow earthquakes, slow slip  
40 event, fault coupling, creeping, and so on. Recently, the role of aseismic slips has been noted  
41 because they show notable interaction with the other slip phenomena. In the Tohoku subduction  
42 zone, Japan, where the 2011 M9 Tohoku earthquake occurred, a long-term aseismic slip event  
43 (L-ASE) was found prior to 2011 and was considered to be one of the precursor of the M9  
44 earthquake. This study newly found a similar L-ASE at the deep plate interface since late 2019  
45 by elaborated GNSS time-series processing techniques. The 2019 L-ASE would be a recurring  
46 event of the previous L-ASE. From the comparison of these L-ASE, possible scenarios suggesting  
47 interaction between the L-ASEs and the other slip phenomena was discussed, and then the L-  
48 ASEs may bring about M7-class seismicity and provide strain accumulation in the M9 rupture  
49 area. Since the 2019 L-ASE may be still ongoing, monitoring of this event and investigation of  
50 its physical role through numerical simulation will be important to assess the hazard risk off  
51 Tohoku in the future.

## 52 **1 Introduction**

53  
54 Various slip behaviors have been documented along plate interfaces, such as interplate  
55 earthquakes (e.g., Suito et al., 2011; Iinuma et al., 2011), afterslip (e.g., Suito et al., 2011; Iinuma  
56 et al., 2016), slow-slip events (SSEs) (e.g., Schwartz & Rokosky, 2007), and slow earthquakes  
57 (e.g., Schwartz & Rokosky, 2007; Obara & Kato, 2016; Nishikawa et al., 2019). SSEs have  
58 various characteristics, including regular SSEs (e.g., Hirose et al., 2011) and SSEs accompanying  
59 earthquake swarms (e.g., Villegas-Lanza et al., 2015; Uchida et al., 2016; Nishikawa et al.,  
60 2019). Moreover, long-term (decadal) aseismic slip events (L-ASEs), which may be considered  
61 as a temporal decrease in the interplate coupling, have been reported (Yokota & Koketsu, 2015;  
62

63 Mavrommatis et al., 2015; Tsang et al., 2015). The diversity of slip behaviors suggests a spatial  
64 variation in frictional properties (e.g., Miyazaki et al., 2004; Nakata et al., 2012). Slip behaviors  
65 are quite different among subduction zones (Nishikawa et al., 2019); thus, compiling slip  
66 phenomena in subduction zones is important to assess frictional properties and future seismic  
67 hazard (Nakata et al., 2016; Nishikawa et al., 2023).

68 The Tohoku subduction zone along Japan Trench has experienced various slips, such as  
69 the 2011  $M_w$ 9.0 Tohoku-oki earthquake (hereafter, referred to as the Tohoku earthquake), M7  
70 class interplate earthquakes, their afterslips (Suito et al., 2011), SSEs with repeating earthquakes  
71 and/or earthquake swarms (Uchida et al., 2016; Nishikawa et al., 2019; Honsho et al., 2019), and  
72 slow earthquakes (Nishikawa et al., 2019). In addition, remarkable slip behavior in the Tohoku  
73 subduction zone was L-ASE prior to the Tohoku earthquake (Yokota & Koketsu, 2015;  
74 Mavrommatis et al., 2015), which occurred from 2002 until the occurrence of the Tohoku  
75 earthquake in the downdip of rupture area of the Tohoku earthquake. The 2002 L-ASE provided  
76 stress accumulation in the rupture area of the Tohoku earthquake and was interpreted as a  
77 possible precursor to the large interplate earthquake. However, small-scale aseismic slips, such  
78 as SSEs, afterslips of M7 class earthquakes and L-ASE, after the Tohoku earthquake have not  
79 been well-investigated because of the evident postseismic deformation of the Tohoku earthquake  
80 (Iinuma et al., 2016; Tomita et al., 2020).

81 This study investigated small-scale aseismic slips using onshore Global Navigation  
82 Satellite Service (GNSS) sites after the 2011 Tohoku earthquake. Subsequently, afterslip  
83 distributions of M7 class interplate earthquakes and a possible L-ASE from late 2019 were  
84 reported. Considering these new findings, the slip behavior off Tohoku was discussed.

85

## 86 **2 Data and Methods**

### 87 **2.1 Data and pre-processing**

88 GNSS Earth Observation Network System (GEONET) F5 daily solutions for the East-  
89 West (EW), North-South (NS), and Up-Down (UD) components, which are distributed by  
90 Geospatial Information Authority of Japan (GSI) (Takamatsu et al., 2023), were employed as  
91 raw GNSS time-series data in this study. The data collection period was from March 12, 2011, to  
92 November 20, 2021. The employed observational sites were 213 GEONET sites, which have  
93 over 3000 daily solutions, were located within the latitudes of 36–42° and longitudes of 139–  
94 142° (Figure 1).

95 The raw GNSS data were considered to include the following factors: (a) postseismic  
96 deformation of the 2011 Tohoku-oki earthquake, (b) offsets due to earthquakes after the 2011  
97 Tohoku-oki earthquake and GNSS antenna maintenance, (c) postseismic deformation of large  
98 earthquakes after the 2011 Tohoku-oki earthquake, (d) common mode error (CME), (e) periodic  
99 variation, and (f) other crustal deformation factors. The preprocessing method of this study  
100 excluded factors (a), (b), (d), and (e) to examine the afterslip of large earthquakes after the 2011  
101 Tohoku-oki earthquake and other aseismic slip events. The earthquake catalog after the 2011  
102 Tohoku-oki earthquake was obtained from the F-net earthquake catalog (Okada et al., 2004) at  
103 latitudes of 32–44°, longitudes of 136–148°, and magnitudes larger than 5.0. The preprocessing  
104 steps are as follows, and Figure 2 shows an example of the pre-processing results for the EW  
105 component of site 950167 (Yamada, Iwate prefecture).

106 First, the contributions of postseismic deformation due to the 2011 Tohoku-oki  
 107 earthquake (a) were modeled. Postseismic deformation due to a large earthquake can be modeled  
 108 by logarithm and/or exponential functions (e.g., Bevis & Brown, 2014). For modeling (a), it is  
 109 preferable to employ a combination of two logarithmic functions and one exponential function  
 110 (Fujiwara et al., 2022). Placing the raw GNSS time-series for the  $k$ th component of the  $n$ th site  
 111 as  $D_{n,k}^{\text{raw}}(t)$  with time (days) of  $t$ , contributions (a) and (b) are modeled as follows:

$$D_{n,k}^{\text{raw}}(t) = D_{n,k}^{\text{ini}}(t) + \sum_{l=1}^{L_n} h_l H(t - t_l) + \epsilon_{n,k}(t) \quad (1)$$

112 with

$$D_{n,k}^{\text{ini}}(t) = a_{n,k} + b_{n,k}t + c_{n,k} \log(1 + t/\tau_1) + d_{n,k} \log(1 + t/\tau_2) + e_{n,k}(1 - \exp(-t/\tau_3)) \quad (2)$$

113 where  $H$  is a Heaviside step function,  $\tau_1$ ,  $\tau_2$ , and  $\tau_3$  are the relaxation times expressing the  
 114 postseismic deformation of the 2011 Tohoku-oki earthquake ( $\tau_1 = 1.59$ ,  $\tau_2 = 148.6$ , and  
 115  $\tau_3 = 3645$  days; Fujiwara et al., 2022), and  $\epsilon_{n,k}(t)$  indicates the residual time-series.  $t_l$   
 116 represents the day of occurrence of an offset event, and  $L_n$  represents the total number of offset  
 117 events for the  $n$ th site. An earthquake with an epicenter within the threshold distance was  
 118 considered an offset event. The threshold distance  $r_0$  depends on the moment magnitude, as with  
 119 Ikuta et al. (2012):

$$r_0 = \begin{cases} 10^{M_w-4.3} & \text{if } M_w \geq 6.8 \\ 10^{M_w/2-0.9} & \text{if } M_w < 6.8 \end{cases} \quad (3).$$

120 In addition, GNSS antenna maintenance was included as an offset event, which is listed in the  
 121 maintenance table distributed by the GSI. The unknown parameters in Eqs. 1 and 2 ( $a_{n,k}$ ,  $b_{n,k}$ ,  
 122  $c_{n,k}$ ,  $d_{n,k}$ ,  $e_{n,k}$ , and  $h_l$ ) were estimated using the least-squares method. When multiple offset  
 123 events were detected within 3 d, these events were compiled as a single offset event, and the  
 124 occurrence time of the compiled event was set as the earliest time among the events. The black  
 125 and red curves show the raw and modeled time-series using Eq. 1 in Figure 2a.

126 Second, the contribution of the CME (d), which is a common bias among GNSS sites,  
 127 was modeled by stacking detrended GNSS time-series (Widowski et al., 1997). Here, Seasonal  
 128 and Trend decomposition using Loess (STL) analysis (Cleveland et al., 1990) was performed to  
 129 obtain the trend of the GNSS time-series as follows:

$$D_{n,k}^{\text{raw}}(t) - D_{n,k}^{\text{ini}}(t) = S_{n,k}(t) + T_{n,k}(t) + \epsilon_{n,k}(t) \quad (4)$$

130 where  $S_{n,k}(t)$  and  $T_{n,k}(t)$  are the seasonal and trend components, respectively. Then, the CME  
 131 for each day  $CME_k(t)$  was calculated as the 20% trimmed mean of  $D_{n,k}^{\text{raw}}(t) - D_{n,k}^{\text{ini}}(t) - T_{n,k}(t)$   
 132 for a robust estimation. The gray and black plots in Figure 2b show the input time-series  
 133 ( $D_{n,k}^{\text{raw}}(t) - D_{n,k}^{\text{ini}}(t)$ ) and the time-series after removing the CMEs ( $D_{n,k}^{\text{raw}}(t) - D_{n,k}^{\text{ini}}(t) -$   
 134  $CME_k(t)$ ), respectively. The red curve in Figure 2b shows the trend component estimated by  
 135 STL analysis.

136 Third, the contribution of offset events (b) was examined. Although the offset events  
 137 were investigated in the first step, they included postseismic displacements and CMEs. To

138 extract pure offsets, the GNSS time-series after removing CME  $D_{n,k}^{\text{raw}}(t) - D_{n,k}^{\text{ini}}(t) - \text{CME}_k(t)$   
 139 was divided into multiple time windows by the occurrence timings of the offset events, and the  
 140 time-series for each time window was fitted by polynomial functions. The offset between two  
 141 consecutive fitted time-series is the pure offset. For the polynomial functions, maximally 6-order  
 142 of the polynomial function were employed, and the optimal order for each time window was  
 143 determined by the AIC (Akaike's Information Criterion) value (Akaike, 1973). The red and  
 144 orange curves in Figure 2c show the fitting curves of the polynomial functions and the offset  
 145 time-series, respectively.

146 Fourth, the contributions of CMEs (d) and offset events (b) were re-examined because  
 147 these contributions may affect each other; therefore, the second and third steps were repeated.  
 148 Placing the calculated offset time-series in the third step as  $O_{n,k}(t)$ , the STL analysis was re-  
 149 performed for  $D_{n,k}^{\text{raw}}(t) - D_{n,k}^{\text{ini}}(t) - O_{n,k}(t)$ , and the CMEs were re-obtained as  $\text{CME}'_k(t)$   
 150 through the second step. Then, the third step was re-performed for  $D_{n,k}^{\text{raw}}(t) - D_{n,k}^{\text{ini}}(t) -$   
 151  $\text{CME}'_k(t)$ , and the offset time-series was re-obtained as  $O'_{n,k}(t)$ .

152 Fifth, the contribution of the periodic variation (e) was examined using fast Independent  
 153 Component Analysis (ICA) (Hyvarinen & Oja, 2000). Periodic variation is generally considered  
 154 seasonal and has often been modeled by trigonometric functions with annual and semi-annual  
 155 periods (Bevis & Brown, 2014). However, the seasonal variations are not necessarily stationary.  
 156 Thus, this study handled the periodic components extracted from the fast ICA as periodic  
 157 variations. Before performing the fast ICA, the other factors are maximally eliminated from the  
 158 time-series in advance; here, the GNSS time-series  $D_{n,k}^{\text{raw}}(t) - D_{n,k}^{\text{ini}}(t) - \text{CME}'_k(t) - O'_{n,k}(t)$  is  
 159 modeled by the 8th order polynomial function and the exponential function following the  
 160 occurrence of the earthquakes with the moment magnitude larger than 6.7 as:

$$\begin{aligned}
 & D_{n,k}^{\text{raw}}(t) - D_{n,k}^{\text{ini}}(t) - \text{CME}'_k(t) - O'_{n,k}(t) & (5) \\
 & = \sum_{i=0}^8 f_{n,i} t^i + \sum_{l=1}^{L'_n} g_{n,l} \left[ 1 - \exp \left\{ -\frac{t - t_l}{\tau'_l} \right\} \right] H(t - t_l) + \epsilon_{n,k}(t)
 \end{aligned}$$

161 where  $L'_n$  is the total number of large earthquakes, and  $f_{n,i}$  and  $g_{n,l}$  are unknown parameters for  
 162 this equation. Exponential functions correspond to the post-seismic deformation of large  
 163 earthquakes.  $\tau'_l$  is the relaxation time of the postseismic deformation for each large earthquake,  
 164 which is given using the moment magnitude as  $\tau'_l = 10^{M_w - 5.1}$ . The relaxation time settings  
 165 were determined through trial and error. The fast ICA was applied to the residual time-series  
 166  $\epsilon_{n,k}(t)$  in Equation 5 for all components and all sites. Missing values in the residual time-series  
 167 were interpolated by PPCA (probabilistic Principal Component Analysis) (Stacklies et al., 2007)  
 168 before performing fast ICA. The results of the fast ICA with 20 independent components are  
 169 shown in Figures S1 and S2. Assuming that the independent components of 1, 2, 4, 7, 8, 10, 12,  
 170 13, 14, 15, 18, and 19 demonstrated periodic variations, these components were summed. An  
 171 example of the summated time-series is shown as a black plot in Figure 2d. Considering that the  
 172 periodic variation should be continuous in time, the 3d Spline smoothing function was fitted to  
 173 the summated time-series, as shown by the red curve in Figure 2d, and the smoothed time-series  
 174 were handled as the periodic variation.

175 Sixth, the contributions of offset events (b) were re-examined by considering the above  
 176 periodic variation. The third step was re-performed for  $D_{n,k}^{\text{raw}}(t) - D_{n,k}^{\text{ini}}(t) - CME'_k(t) -$   
 177  $P_{n,k}(t)$ , and the offset time-series was re-obtained as  $O''_{n,k}(t)$ . where  $P_{n,k}(t)$  are the periodic  
 178 variations obtained in the fifth step. An example of the results estimated in this step is shown in  
 179 Figure 2e. Moreover, a comparison between the estimated offsets and calculated displacements  
 180 based on Global CMT solutions (Dziewonski et al., 1981; Ekström et al., 2012) assuming a  
 181 uniform elastic half-space (Okada, 1992) is shown in Figures S3 and S4. As the estimated offsets  
 182 and the calculated displacements are comparable with each other except the earthquakes on Jul.  
 183 10, 2011 and Oct. 25, 2013, the offsets were considered to be well obtained in this pre-  
 184 processing. As the exceptional two earthquakes were relative far-field events and provided  
 185 similar displacements among the observational sites (Figures S3c and S3h), the coseismic signals  
 186 might be removed as CME. These figures only show the results of the offset earthquake events,  
 187 where the maximum calculated displacements are over 2.5 mm. Although the offsets were  
 188 estimated for other earthquakes, the obtained offset displacements for those earthquakes  
 189 generally showed random displacement fields, suggesting observational noise; thus, the  
 190 estimated offsets for those events did not exceed the observational noise level and did not affect  
 191 the trajectory modeling performed in the next section.

192 Finally, the pre-processed GNSS time-series  $D_{n,k}(t)$  were obtained as  $D_{n,k}(t) =$   
 193  $D_{n,k}^{\text{raw}}(t) - CME'_k(t) - O''_{n,k}(t) - P_{n,k}(t)$ . An example of a pre-processed time-series is shown  
 194 in Figure 2f.

195

## 196 2.2 GNSS site segmentation and trajectory modeling

197 Time-series stacking of multiple GNSS sites has often been conducted to suppress the  
 198 effects of noise and highlight the effects of crustal deformation (e.g., Takagi et al., 2019).  
 199 However, stacking too many sites may mask local crustal deformation. Here, segmentation of the  
 200 GNSS sites was first conducted, and then averaging of the time-series for each segmented group  
 201 was performed.

202 Before performing segmentation, the dominant contributions of the 2011 Tohoku-oki  
 203 earthquake were removed by modeling  $D_{n,k}(t)$  as  $D_{n,k}^{\text{post}}(t)$ .  $D_{n,k}^{\text{post}}(t)$  has the same formula as  
 204 that in Equation (2). An example of fitting by  $D_{n,k}^{\text{post}}(t)$  is shown by the red curve in Figure 2f,  
 205 and the cumulative displacements due to  $D_{n,k}^{\text{post}}(t)$  are shown in Figure 3. Using the residual  
 206 time-series, k-means cluster analysis was performed for segmentation. The total number of  
 207 clusters was set to 18 so that the number of sites for each group was more than five. The latitude  
 208 and longitude for each site were added to the end of the residual time-series in advance because  
 209 spatially separated sites were determined to be in the same group without this process. The  
 210 stacked time-series  $D_{m,k}^{\text{Stack}}(t)$  ( $m$ : the group number) was calculated as the average of the  
 211 residual time-series and was obtained for each component of each group. The segmented groups  
 212 and stacked time-series for each group are shown in Figures 4–6.

213 The stacked time-series were modeled by the following two approach, Model-1 and  
 214 Model-2. The reasons why these two approaches were employed were discussed in Section 3.1.  
 215 Model-1 includes the postseismic deformation of the 2011 Tohoku-oki earthquake, postseismic  
 216 deformations due to large earthquakes with moment magnitudes larger than 6.7, and the 2011

217 and 2018 Boso SSEs (Ozawa et al., 2019). Although the stacked time-series already excluded the  
 218 post-seismic deformation of the 2011 Tohoku-oki earthquake, it was also re-included considering  
 219 its interaction with other factors. The 2014 Boso SSE also occurred in December 2013; however,  
 220 its equivalent magnitude was relatively smaller than that of the 2011 and 2018 events so the  
 221 displacements due to the 2014 event were not considered. Model-1 is given as follows:

$$D_{m,k}^{\text{Model-1}}(t) = D_{m,k}^{\text{Post}}(t) + \sum_{l=1}^{L'_m} g_{m,l} \left[ 1 - \exp \left\{ -\frac{t-t_l}{\tau'_l} \right\} \right] H(t-t_l) \quad (6)$$

$$+ \sum_{j=1}^{J_m} h_{m,j} \hat{R}(t_j, T_j)$$

222 with

$$\hat{R}(t_j, T_j) = \frac{R(t_j)}{T_j} - \frac{R(t_j + T_j)}{T_j} \quad (7)$$

223 where  $R(t)$  denotes the ramp function. The first term on the right-hand side represents the  
 224 postseismic deformation of the 2011 Tohoku-oki earthquake, as shown in Equation 2: The  
 225 second term on the right-hand side represents postseismic deformations due to large earthquakes  
 226 with moment magnitudes greater than 6.7. The relaxation time  $\tau'_l$  is given as  $\tau'_l = 10^{M_w-4.7}$  for  
 227 the interplate earthquakes and  $\tau'_l = 10^{M_w-5.5}$  for the other types of earthquakes; the parameters  
 228 for the index (4.7 and 5.5) were optimized to minimize the residuals of all groups. The third  
 229 terms on the right-hand side represent the 2011 ( $j = 1$ ) and 2018 ( $j = 2$ ) Boso SSEs, where  $t_j$   
 230 and  $T_j$  are the onset time and duration of each SSE (Ozawa et al., 2019), respectively. This term  
 231 was applied only to the southernmost group ( $m = 8,16$ ).

232 Model-2 contains the 2019 L-ASE term in addition to Model-1 as:

$$D_{m,k}^{\text{Model-2}}(t) = D_{m,k}^{\text{Model-1}}(t) + q_m \hat{R}(t_{\text{LASE}}, T_{\text{LASE}}) \quad (8)$$

233 where  $t_{\text{LASE}}$  and  $T_{\text{LASE}}$  are the onset time and duration of the L-ASE, respectively. Because it is  
 234 difficult to optimize the ending time of L-ASE, only  $t_{\text{LASE}}$  was optimized and determined to be  
 235 November 25, 2019, by minimizing the residuals of all groups. This term was applied to all  
 236 groups and  $T_{\text{LASE}}$  was set as the ending time corresponding to the end of the entire data period.

237 Then, to obtain displacements due to postseismic deformations following large  
 238 earthquakes with moment magnitudes larger than 6.7, and the L-ASE for each site, Model-2 was  
 239 also applied to the individual (not stacked) GNSS time-series for the  $k$ th component of the  $n$ th  
 240 site as

$$D_{n,k}(t) = D_{n,k}^{\text{Model-2}}(t) + \epsilon_{n,k}(t) \quad (9).$$

241

### 242 2.3 Aseismic slip inversion method

243 To estimate the aseismic slip distributions, a geodetic slip inversion based on a non-  
 244 negative least-squares method with Laplacian regularization was performed with the  
 245 hyperparameter of regularization optimized by Akaike's Bayesian Information Criterion (ABIC)

246 (Akaike, 1980; Yabuki & Matsu'ura, 1992). Green's functions were obtained from the Green's  
247 function library for the Tohoku region, assuming a 3D elastic underground structure (Hori et al.,  
248 2021). The library expresses the plate interface by 3-dimensional B-spline functions, and the  
249 node points for the 3-dimensional B-spline functions are shown by gray circles in Figure 1. Zero-  
250 slip constraints for the southern, northern, and down-dip edges were also considered when  
251 providing Laplacian regularization (e.g., Zhou et al., 2014). The observational errors for the data  
252 covariance matrix assumed a diagonal matrix and the diagonal components were given as the  
253 model variances of the least-squares method in the trajectory modeling.

254 The slip inversion was performed for the afterslips of the major earthquakes (moment  
255 magnitude of 6.7 or greater) after 2012 and the 2019 L-SAE. Several large interplate earthquakes  
256 occurred in 2011. However, because large earthquakes occurred consecutively for the first 1 year  
257 after the 2011 Tohoku earthquake, the trajectory model failed to separately model the  
258 postseismic deformations of individual large earthquakes because of their trade-off relationship.  
259 Hence, these events were not examined in this study. Fully relaxed postseismic displacements,  
260 which were the coefficients of the exponential functions in Model-2, were employed as the input  
261 data for the inversion.

262

### 263 **3 Results**

#### 264 3.1 Trajectory modeling of GNSS time-series

265 Figure 4b–d show stacked GNSS time-series for the individual site groups (Figure 4a)  
266 after the preprocess that eliminated postseismic deformation due to the 2011 Tohoku earthquake,  
267 offsets due to earthquakes and antenna maintenance, periodic variation, common mode errors,  
268 and constant plate motion from the raw GNSS time-series. While Figure 4 shows the results for  
269 site groups along the coastline, Figures 5 and 6 show those for the other groups.

270 The stacked GNSS time-series were firstly modeled by a combination of postseismic  
271 deformations of large earthquakes (moment magnitude of 6.7 or greater) and the 2011 and 2018  
272 Boso SSEs using the trajectory fitting technique (Model-1, magenta curves in Figure 4b–d),  
273 which were modeled by exponential functions and ramp functions, respectively. The residuals of  
274 Model-1 for the horizontal components (magenta plots in Figure 4e–f) exhibited significant  
275 deviations from late 2019 to early 2021 in the central and southern Tohoku regions (Figures 4–  
276 6). Assuming that the deviation was driven by an unknown transient event, a ramp function was  
277 employed to model it, and its onset was estimated to be November 25, 2019. The ending time  
278 was set to the end of the data period because it was not properly optimized owing to the trade-off  
279 relationship with the postseismic deformations of the M7 class earthquakes on February 13,  
280 March 20, and May 1, 2021. The cyan curves in Figure 4b–d show the GNSS time-series  
281 modeled by Model-2, which considered the ramp function in addition to Model-1. Both Model-1  
282 and Model-2 reproduced the observed GNSS time-series to a similar degree until the first half of  
283 2019 (Figure 4e–f). Additionally, Model-2 successfully reproduced the time-series after late  
284 2019 to a degree comparable to that of the former period. The dotted lines indicate  $2\sigma$  error range  
285 of the Model-2 residuals, and it is confirmed that the deviation due to the transient movement in  
286 Model-1 was significant beyond the error range. The transient movement may be initiated  
287 gradually, unlike the ramp function; however, it is difficult to assess its initiation process  
288 considering data noises.

289

## 290 3.2 Slip distributions of the aseismic slip events

291 The black arrows in Figure 7a–c show the fully relaxed post-seismic horizontal  
292 displacements of major interplate earthquakes with a moment magnitude of 6.7 or greater that  
293 occurred after 2012. The vertical red and blue bars in Figure 8a–c show the fully relaxed post-  
294 seismic vertical displacements. Figures 7a and 8a show the postseismic displacement fields of  
295  $M_w$ 6.73 Sanriku-oki earthquake on February 16, 2015, and Figures 7b and 8b show those of  
296  $M_w$ 6.81 Miyagi-oki earthquake on May 12, 2015. Figures 7c and 8c show the summation of the  
297 postseismic displacement fields of the  $M_w$ 7.10 Fukushima-oki (February 13, 2021),  $M_w$ 7.06  
298 Miyagi-oki (March 20, 2021), and  $M_w$ 6.85 Miyagi-oki (May 1, 2021) earthquakes because the  
299 contributions of these earthquakes were mixed owing to their trade-off relationship. Although the  
300 first Fukushima-oki earthquake was an intraslab earthquake, the post-seismic deformations of the  
301 later Miyagi-oki earthquakes were considered dominant because the displacements in Miyagi  
302 (approximately N38.5°) were larger than those in Fukushima (approximately 37.5°N).

303 The postseismic displacements in Figures 7a–c are considered to demonstrate afterslip  
304 because afterslip is a dominant process in postseismic deformation when the moment magnitude  
305 of a mainshock is less than 7.5 (Sun & Wang, 2015). Therefore, afterslip distributions were  
306 estimated from the post-seismic displacements using the geodetic slip inversion method in Figure  
307 7a–c. As the results of the inversion, Figures 8a–c show the estimation errors, and Figures 8e–f  
308 show the estimated slip over the  $2\sigma$  estimation error for the inversion node points. The calculated  
309 postseismic displacements are shown by blue arrows in the horizontal components (Figure 7a–c)  
310 and by magenta and cyan bars (Figure 8a–c) in the vertical component. While the horizontal  
311 calculated displacements largely fitted to the observations, the vertical calculated displacements  
312 are much smaller than the observations. As the observed vertical displacements show spatially  
313 random amounts, it is considered to be difficult to obtain the vertical postseismic displacements  
314 by the trajectory modeling, because of the observational noises. Considering this matter, the  
315 inversion results were mostly provided to explain the observed horizontal motions.

316 The afterslip of 2015  $M_w$ 6.73 Sanriku-oki earthquake was broadly estimated on the  
317 shallow plate interface around N40° (Figure 7a), and the equivalent moment magnitude was  
318  $M_w$ 7.17 ( $7.18 \times 10^{19}$  Nm). This large moment release compared with the coseismic rupture  
319 includes contributions from an SSE, which was reported by a seafloor geodetic and small  
320 repeating earthquake study (Honsho et al., 2019) with a spatially compact slip of over 20 cm.  
321 The estimated afterslip distribution may be oversmoothed by insufficient sensitivity to reproduce  
322 shallow slip. The afterslip of the 2015  $M_w$ 6.81 Miyagi-oki earthquake was estimated to be in the  
323 downdip portion of the mainshock (Figure 7b), and the equivalent moment magnitude was  
324  $M_w$ 6.96 ( $3.50 \times 10^{19}$  Nm). The cumulative afterslip of 2021  $M_w$ 7.06 and  $M_w$ 6.85 Miyagi-oki  
325 earthquakes was estimated in the downdip portion of the mainshocks (Figure 7c), and the  
326 equivalent moment magnitude was  $M_w$ 7.21 ( $8.12 \times 10^{19}$  Nm). Although a slip was also  
327 estimated at N40.5°, it could be artificial considering the estimation error (Figure 8g).

328 The black arrows in Figure 7d show the cumulative displacements modeled by the ramp  
329 functions after November 25, 2019. The displacements generally demonstrated a trench-normal  
330 direction, and the displacements along the eastern coastline were larger than those along the  
331 back-arc area. Therefore, it is considered that this transient motion was driven by an L-ASE and  
332 the slip distribution of this event was also estimated the geodetic inversion method. The

333 inversion results are summarized in Figures 7d, 8d, and 8h by the same manner with the other  
334 afterslip events in Figures 7 and 8. The slip distribution of this L-ASE event was estimated on  
335 the deep and shallow portions of the plate interface (Figure 7d), and the equivalent moment  
336 magnitude was  $M_w 7.55$  ( $2.67 \times 10^{20}$  Nm). However, considering the estimation errors (Figure  
337 8d and 8h), the shallow slip was insignificant. Moreover, a small-scale deep slip was estimated at  
338 the northernmost area around  $N41^\circ$ , but it is difficult to guarantee its meaningfulness because  
339 artificial slips tend to occur at the edge of the analysis domain and because large displacements  
340 are not observed above this slip. Hence, this study only assessed the deeper aseismic slip of  
341  $N37\text{--}39.5^\circ\text{N}$ . The equivalent moment magnitude of the L-ASE is  $M_w 7.35$  ( $1.34 \times 10^{20}$  Nm),  
342 and this event is consistent with the scaling law of seismic moment and duration (Ide et al.,  
343 2007) although the ending time of this event has currently not been well-identified.

344

## 345 **4 Discussion**

### 346 4.1 Spatial extent of L-ASEs

347 Various slip behaviors along Japan Trench (Nagai et al., 2001; Igarashi et al., 2001;  
348 Yamanaka & Kikuchi, 2003; Murotani et al., 2003; Yamanaka & Kikuchi, 2004; Inuma et al.,  
349 2012; Yokota & Koketsu, 2015; Inuma et al., 2016; Nakamura et al., 2016; Satake et al., 2017;  
350 Nishikawa et al., 2019; Nishimura, 2021) are summarized in Figure 9a, with the afterslips (blue  
351 contours) and the 2019 L-ASE (green contours) areas estimated in this study. The plate  
352 interface depth of the slip peaks of the 2019 L-ASE was approximately 60 km, which is deeper  
353 than that of any other slip phenomenon including the afterslip areas of the 2021 Miyagi-oki  
354 earthquakes. This depth corresponds to the depth at which aseismic slips are likely to occur due  
355 to the water supply (Nishikawa et al., 2023). As with the 2002 L-ASE (purple contours; Yokota  
356 & Koketsu, 2015), an obvious increase in seismicity was not observed at the initiation of the L-  
357 ASE, suggesting that the L-ASE spontaneously occurred where seismic activity could not  
358 appear. Because the estimated depth is greater than the downdip limit of interplate earthquakes  
359 (red dotted curve; Igarashi et al., 2001), the absence of seismicity at the initiation of the L-ASE  
360 supports the estimated depth.

361 Although the 2019 L-ASE was estimated to be in the downdip portion of the 2002 L-  
362 ASE, its spatial relationship remains controversial. The inversion results were not sufficiently  
363 sensitive to the shallower portion but demonstrated shallow slip (Figure 7d), which might  
364 suggest that the 2019 L-ASE possibly extended the shallower portion similar to the 2002 L-ASE.  
365 Moreover, spatial extent of the 2002 L-ASE includes M7 class earthquakes at the depth of  
366 approximately 20–40 km (e.g., Suito et al., 2011); the previous studies excluded postseismic  
367 deformations of those events (Yokota & Koketsu, 2015; Mavrommatis et al., 2015), the 2002 L-  
368 ASE distribution possibly included contributions of their afterslips and was estimated in the  
369 shallower portion. Considering these issues, it is difficult to determine whether the 2002 and  
370 2019 L-ASEs were spatially complementary or overlapping. If they overlapped, the 2019 L-ASE  
371 may have been a recurring event in the 2002 L-ASE. Otherwise, the strains were released  
372 independently at different depths. In both cases, such an L-ASE is not a special event which  
373 occur just prior to the M9 megathrust earthquake but can occur even  $\sim 8$  years after the M9  
374 earthquake off Tohoku.

375 In the along-trench direction, the extent of L-ASE was determined to be better than that  
376 in the dip direction because of the site distribution (Figure 8d). In the northern and southern  
377 regions of the L-ASEs, deep aseismic slip events were found as afterslips of the Tohoku  
378 earthquake (cyan shaded region in Figure 9a; Iinuma et al., 2016) and repeated SSEs (green open  
379 circles in Figure 9a; Nishimura, 2021), respectively. Both the 2002 and 2019 L-ASEs  
380 compensated for deep aseismic slip in the along-trench direction and contributed to the release of  
381 strain at the deep plate interface.

382

#### 383 4.2 Strain release process off Tohoku

384 Considering the locational uncertainty of the 2002 and 2019 L-ASEs, three cases of the  
385 strain release process associated with the L-ASEs have been suggested. Case-1: two spatially  
386 complementary slip domains exist, which are the very deep (2019 type) and deep (2002 type) L-  
387 ASEs and work individually (Figure 9b). Case-2: the very-deep L-ASE exists alone (Figure 9c);  
388 Case-3: the very-deep and deep L-ASEs work simultaneously (Figure 9d). The very-deep L-ASE  
389 exists independently of the other slips, whereas the deep L-ASE partially overlaps with medium-  
390 scale interplate earthquakes and their afterslips.

391 Assuming that both very-deep and deep L-ASEs occur repeatedly, they commonly have  
392 the following possible features, regardless of the above cases. First, slip rates of these L-ASEs  
393 (approximately 4 cm/yr and 6.5 cm/yr in this study and Yokota & Koketsu (2015), respectively)  
394 are lower than the maximum slip deficit rate (approximately 8 cm/yr), which suggests low strain  
395 accumulation rates during the inter-L-ASE period. Thus, partial or weak coupling due to the  
396 stress shadow of shallower locking may appear during the inter-L-ASE period. Second, L-ASEs  
397 may precede M7 class interplate earthquakes. This feature has already been suggested in an  
398 earthquake cycle simulation (Yokota & Koketsu, 2015). Actually, M7 class interplate  
399 earthquakes occurred after the initiation of the 2002 L-ASE (e.g., the 2005 August 16 Miyagi,  
400 2008 May 8 Ibaraki, 2008 July 19 Fukushima earthquakes; magenta stars in Figure 9a), whereas  
401 no major earthquakes occurred during 1996–2002, and the 2021 Miyagi-oki earthquakes  
402 occurred after the initiation of the 2019 L-ASE. Additionally, it is well-known that M7 class  
403 earthquakes have repeatedly occurred in an interval of 30–40 years off Tohoku (e.g., Nakata et  
404 al., 2016), and conventional geodetic data suggest the possibility that onshore strain  
405 accumulation rates have temporal fluctuations with similar periodicity (Meneses-Gutierrez et al.,  
406 2022). These activities prior to 2002 were possibly triggered by the past L-ASEs. It was reported  
407 that SSEs promote intraslab earthquakes via water transportation in the Nankai subduction zone  
408 (Kita et al., 2021). Although intraslab earthquakes occurred following the 2002 and 2019 L-ASE  
409 (the 2003 May 26 Miyagi-oki earthquake, the 2021 Fukushima-oki earthquake, and the 2022  
410 March 16 Fukushima-oki earthquake), the relationship between L-ASEs and intraslab  
411 earthquakes is beyond the range of this study, and it should be investigated carefully in the  
412 future. Finally, the L-ASEs are spatially complementary to the M9 rupture area; they contribute  
413 to enhancing stress accumulation in the M9 rupture area because Coulomb stress changes caused  
414 by an L-ASE promote stress accumulation in the updip portion of the L-ASE (Yokota &  
415 Koketsu, 2015).

416 Case-2 is the simplest scenario, in which a very-deep L-ASE occurs repeatedly, triggers  
417 M7 class earthquakes and their afterslips, and accumulates stress in the M9 rupture area. Case-3  
418 indicates that the deep L-ASE also repeatedly occurs with the very deep L-ASE and has a similar

419 influence as in Case-2. However, the deep L-ASE collocates with the other slips; thus, the spatial  
420 complexity of the deep plate interface and the interaction between the L-ASE and the collocated  
421 slips should be considered. In Case-1, very deep and deep L-ASEs occur individually and  
422 repeatedly, which affect the shallower plate interface, as in Cases 2 and 3. In addition to the  
423 spatial complexity of the deep plate interface, the interaction between very deep and deep L-  
424 ASEs should be considered. They may stimulate each other and occasionally occur  
425 simultaneously. The most plausible scenarios should be clarified in the future because these  
426 scenarios would require different patterns of the frictional parameters on the plate interface. In  
427 any case, note that the L-ASEs may stimulate various shallower slips and are possible precursors  
428 of the entire M7 class and M9 seismicity.

429

## 430 **5 Conclusions**

431 This study processed the onshore GNSS data by the elaborated data-cleaning methods,  
432 the stacking approach, and the trajectory modeling approach, and then revealed various small-  
433 scale aseismic slip events (afterslips of M7-class earthquakes and an L-ASE since late 2019)  
434 which had been hidden by a massive postseismic deformation of the 2011 M9 Tohoku  
435 earthquake. The afterslip distributions of the 2015  $M_w$ 6.73 Sanriku-oki earthquake, the 2015  
436  $M_w$ 6.81 Miyagi-oki earthquake, and the 2021 M7-class Miyagi-oki earthquakes and the slip  
437 distribution of the 2019 L-ASE were estimated. The 2019 L-ASE is a similar event of the 2002  
438 L-ASE (Yokota & Koketsu, 2015) prior to the 2011 M9 Tohoku-oki earthquake. The 2019 L-  
439 ASE is considered to still be ongoing; if this event is the recurrence event of the 2002 L-ASE, its  
440 duration would be over several years. The slip distribution of the 2019 L-ASE was estimated to  
441 be on the deeper plate interface than any other slip behaviors including the 2002 L-ASE;  
442 however, its possibly extended to the shallower portion as well as the 2002 L-ASE. This  
443 locational uncertainty provides us various scenarios of the repeated occurrence of the L-ASEs off  
444 Tohoku, but in any scenarios, the L-ASEs may occur on the deep plate interface, promote M7-  
445 class seismicity on the shallow plate interface, and provide strain accumulation in the M9 rupture  
446 zone. Thus, it is important to monitor the ongoing L-ASE and seismicity and to assess the  
447 interaction between L-ASEs and other slip behaviors through further numerical simulations in  
448 the future.

449

## 450 **Acknowledgments**

451 I am thankful to the GSI for maintaining the GEONET sites and distributing the F5  
452 solutions, Dr. Hiroaki Kobayashi for providing the slip distributions of the 2002 L-ASE and  
453 afterslip of the 1994 Sanriku earthquake shown in Yokota & Koketsu (2015), and Dr. Ryoichiro  
454 Agata for providing the Green's function library (Hori et al., 2021). The slip distributions of  
455 major interplate earthquakes after the 2011 Tohoku earthquake (red contours in Figure 9a) using  
456 strong-motion seismic waveform records were obtained from the Japan Meteorological Agency  
457 webpage (<https://www.data.jma.go.jp/eqev/data/sourceprocess/index.html>) in Japanese. All  
458 figures were drawn using Generic Mapping Tools (Wessel et al., 2013). This research was  
459 supported by Japan Society for the Promotion of Science (JSPS) KAKENHI (Grant Number:  
460 20K14588).

461

462 **Open Research**

463 The fully relaxed postseismic displacements of the 2015 Feb. 17, 2015 May 13, the 2021,  
 464 earthquakes and the 2019 L-ASE displacements shown in Figures 7 and 8 are listed in Tables S1–4. Other  
 465 data, such as grid files of slip distributions, are available from the authors upon reasonable request.  
 466

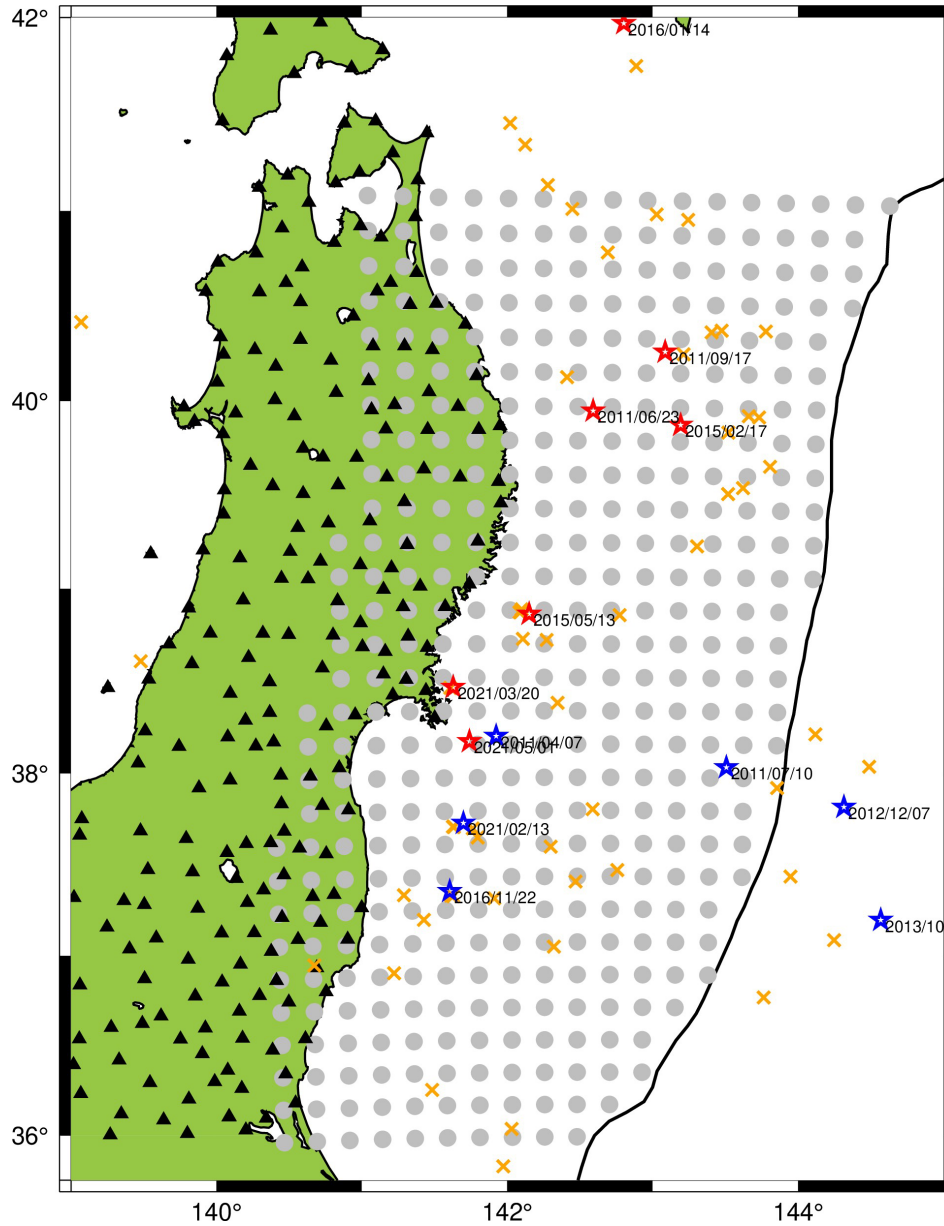
467 **References**

- 468 Akaike, H (1973), Information Theory and Maximum Likelihood Principle. In: Petrov BN, and Csäki F  
 469 (Eds.) 2nd International Symposium on Information Theory. Akademiai Kiado, Budapest.
- 470 Akaike, H (1980), Likelihood and the Bayes procedure, In: Bernardo, J. M., DeGroot, M. H., Lindley, D.  
 471 V., & Smith, A. F. M. (Eds.) Bayesian Statistics, 143–166, University Press, Valencia (1980).
- 472 Bevis, M., & Brown, A (2014), Trajectory models and reference frames for crustal motion geodesy. *J.*  
 473 *Geod.*, 88(3), 283–311. <https://doi.org/10.1007/s00190-013-0685-5>
- 474 Cleveland, R. B., Cleveland, WS, McRae, JE, & Terpenning, I (1990), STL: A seasonal-trend  
 475 decomposition procedure based on loess. *J. Offic. Stat.*, 6, 3–73.
- 476 Dziewonski, A. M., Chou, T. A., & Woodhouse, J. H (1981), Determination of earthquake source  
 477 parameters from waveform data for studies of global and regional seismicity, *J. Geophys. Res.*, 86,  
 478 2825–2852. <https://doi.org/10.1029/JB086iB04p02825>
- 479 Ekström, G., Nettles, M. & Dziewonski, A. M (2012), The global CMT project 2004-2010: Centroid-  
 480 moment tensors for 13,017 earthquakes, *Phys. Earth Planet. Inter.*, 200–201, 1–9.  
 481 <https://doi.org/10.1016/j.pepi.2012.04.002>
- 482 Fujiwara, S., Tobita, M., & Ozawa, S (2022), Spatiotemporal functional modeling of postseismic  
 483 deformations after the 2011 Tohoku-Oki earthquake. *Earth, Planets and Space*, 74(1), 13.  
 484 <https://doi.org/10.1186/s40623-021-01568-0>
- 485 Hirose, H., Asano, Y., Obara, K., Kimura, T., Matsuzawa, T., Tanaka, S., & Maeda, T (2010), Slow  
 486 Earthquakes Linked Along Dip in the Nankai Subduction Zone. *Science*, 330(6010), 1502.  
 487 <https://doi.org/10.1126/science.1197102>
- 488 Honsho, C., Kido, M., Tomita, F., & Uchida, N (2019), Offshore Postseismic Deformation of the 2011  
 489 Tohoku Earthquake Revisited: Application of an Improved GPS-Acoustic Positioning Method  
 490 Considering Horizontal Gradient of Sound Speed Structure. *J. Geophys. Res.*, 124, 5990–6009.  
 491 <https://doi.org/10.1029/2018JB017135>
- 492 Hori, T., Agata, R., Ichimura, T., Fujita, K., Yamaguchi, T., & Iinuma, T (2021), High-fidelity elastic  
 493 Green's functions for subduction zone models consistent with the global standard geodetic reference  
 494 system. *Earth Planets Space*, 73, 41. <https://doi.org/10.1186/s40623-021-01370-y>
- 495 Hyvarinen, A. & Oja, E (2000), Independent Component Analysis: Algorithms and Applications, *Neural*  
 496 *Networks*, 13(4-5), 411–430. [https://doi.org/10.1016/S0893-6080\(00\)00026-5](https://doi.org/10.1016/S0893-6080(00)00026-5)
- 497 Ide, S., Beroza, G. C., Shelly, D. R., & Uchide, T (2007), A scaling law for slow earthquakes. *Nature*,  
 498 447(7140), 76–79. <https://doi.org/10.1038/nature05780>
- 499 Igarashi, T., Matsuzawa, T., Umino, N., & Hasegawa, A (2001), Spatial distribution of focal mechanisms  
 500 for interplate and intraplate earthquakes associated with the subducting Pacific plate beneath the

- 501 northeastern Japan arc: A triple-planed deep seismic zone, *J. Geophys. Res.*, *106*(B2), 2177-2191,  
502 <https://doi.org/10.1029/2000JB900386>
- 503 Iinuma, T., Hino, R., Kido, M., Inazu, D., Osada, Y., Ito, Y., Ohzono, M., Tsushima, H., Suzuki, S.,  
504 Fujimoto, H., & Miura, S (2012), Coseismic slip distribution of the 2011 off the Pacific Coast of  
505 Tohoku Earthquake (M9.0) refined by means of seafloor geodetic data. *J. Geophys. Res.*, *117*,  
506 B07409. <https://doi.org/10.1029/2012JB009186>
- 507 Iinuma, T., Hino, R., Uchida, N., Nakamura, W., Kido, M., Osada, Y., & Miura, S (2016), Seafloor  
508 observations indicate spatial separation of coseismic and postseismic slips in the 2011 Tohoku  
509 earthquake. *Nat. Comm.*, *7*, 13506. <https://doi.org/10.1038/ncomms13506>
- 510 Ikuta, R., Satomura, M., Fujita, A., Shimada, S., & Ando, M (2012), A small persistent locked area  
511 associated with the 2011 Mw9.0 Tohoku-Oki earthquake, deduced from GPS data. *J. Geophys. Res.*,  
512 *117*, B11408. <https://doi.org/10.1029/2012JB009335>
- 513 Kita, S., Houston, H., Yabe, S., Tanaka, S., Asano, Y., Shibutani, T., & Suda, N (2021), Effects of  
514 episodic slow slip on seismicity and stress near a subduction-zone megathrust. *Nat. Comm.*, *12*(1),  
515 7253. <https://doi.org/10.1038/s41467-021-27453-8>
- 516 Nagai, R., M. Kikuchi, & Y. Yamanaka (2001), Comparative study on the source processes of recurrent  
517 large earthquakes in Sanriku-oki Region: The 1968 Tokachi-oki earthquake and the 1994 Sanriku-  
518 oki earthquake, *Zisin*(2), *54*, 267-280. [https://doi.org/10.4294/zisin1948.54.2\\_267](https://doi.org/10.4294/zisin1948.54.2_267)
- 519 Nakamura, W., Uchida, N., & Matsuzawa, T (2016), Spatial distribution of the faulting types of small  
520 earthquakes around the 2011 Tohoku-oki earthquake: A comprehensive search using template  
521 events. *J. Geophys. Res.*, *121*, 2591–2607. <https://doi.org/10.1002/2015JB012584>
- 522 Nakata, R., Hyodo, M., & Hori, T (2012), Numerical simulation of afterslips and slow slip events that  
523 occurred in the same area in Hyuga-nada of southwest Japan. *Geophys. J. Int.*, *190*(2), 1213–1220.  
524 <https://doi.org/10.1111/j.1365-246X.2012.05552.x>
- 525 Nakata, R., Hori, T., Hyodo, M., & Ariyoshi, K (2016), Possible scenarios for occurrence of M~7  
526 interplate earthquakes prior to and following the 2011 Tohoku-Oki earthquake based on numerical  
527 simulation. *Sci. Rep.*, *6*, 25704. <https://doi.org/10.1038/srep25704>
- 528 Nishikawa, T., Matsuzawa, T., Ohta, K., Uchida, N., Nishimura, T., & Ide, S (2019), The slow earthquake  
529 spectrum in the Japan Trench illuminated by the S-net seafloor observatories. *Science*, *365*(6455),  
530 808–813. <https://doi.org/10.1126/science.aax5618>
- 531 Nishikawa, T., Ide, S., & Nishimura, T (2023), A review on slow earthquakes in the Japan Trench. *Progr.*  
532 *Ear. Planet. Sci.*, *10*(1), 1. <https://doi.org/10.1186/s40645-022-00528-w>
- 533 Nishimura, T (2021), Slow Slip Events in the Kanto and Tokai Regions of Central Japan Detected Using  
534 Global Navigation Satellite System Data During 1994–2020. *Geochem. Geophys. Geosys.*, *22*(2),  
535 e2020GC009329. <https://doi.org/https://doi.org/10.1029/2020GC009329>
- 536 Mavrommatis, A. P., Segall, P., Uchida, N., & Johnson, K. M (2015), Long-term acceleration of aseismic  
537 slip preceding the Mw 9 Tohoku-oki earthquake: Constraints from repeating earthquakes. *Geophys.*  
538 *Res. Lett.*, *42*(22), 9717–9725. <https://doi.org/10.1002/2015GL066069>
- 539 Meneses-Gutierrez, A., Segall, P., & Sagiya, T (2022), How Steady is Interseismic Crustal Deformation  
540 in Northeast Japan? Evidence From an Integrated Analysis of Centennial Geodetic Data. *J. Geophys.*  
541 *Res.*, *127*(2), e2021JB023100. <https://doi.org/https://doi.org/10.1029/2021JB023100>
- 542 Miyazaki, S., Segall, P., Fukuda, J., & Kato, T (2004), Space time distribution of afterslip following the  
543 2003 Tokachi-oki earthquake: Implications for variations in fault zone frictional properties.  
544 *Geophys. Res. Lett.*, *31*(6), L06623. <https://doi.org/10.1029/2003gl019410>

- 545 Murotani, T., Kikuchi, M., & Yamanaka, Y (2003), Rupture processes of large Fukushima-oki  
546 earthquakes in 1938., Abstract 2003 Japan Geoscience Union Meeting, S052-003.
- 547 Obara, K., & Kato, A (2016), Connecting slow earthquakes to huge earthquakes. *Science*, 353(6296),  
548 253–258. <https://doi.org/10.1126/science.aaf1512>.
- 549 Okada, Y (1992), Internal deformation due to shear and tensile faults in a half-space, *Bull. Seism. Soc.*  
550 *Am.*, 82(2), 1018–1040. <https://doi.org/10.1785/BSSA0820021018>
- 551 Okada, Y., Kasahara, K., Hori, S., Obara, K., Sekiguchi, S., Fujiwara, H. & A. Yamamoto (2004), Recent  
552 progress of seismic observation networks in Japan –Hi-net, F-net, K-NET, and KiK-net–. *Earth*  
553 *Planet Space*, 56, xv–xxviii. <https://doi.org/10.1186/BF03353076>
- 554 Ozawa, S., Yarai, H., & Kobayashi, T (2019), Recovery of the recurrence interval of Boso slow slip  
555 events in Japan. *Earth, Planets and Space*, 71(1), 78. <https://doi.org/10.1186/s40623-019-1058-y>
- 556 Satake, K., Fujii, Y., & Yamaki, S (2017), Different depths of near-trench slips of the 1896 Sanriku and  
557 2011 Tohoku earthquakes. *Geosci. Lett.*, 4(1), 33. <https://doi.org/10.1186/s40562-017-0099-y>
- 558 Schwartz, S. Y., & Rokosky, J. M (2007), Slow slip events and seismic tremor at circum-pacific  
559 subduction zones. *Reviews of Geophysics*, 45, 3. <https://doi.org/10.1029/2006RG000208>
- 560 Stacklies, W., Redestig, H., Scholz, M., Walther, D., & Selbig, J (2007), pcaMethods—a bioconductor  
561 package providing PCA methods for incomplete data, *Bioinformatics*, 23, 9, 1164–1167.  
562 <https://doi.org/10.1093/bioinformatics/btm069>
- 563 Suito, H., Nishimura, T., Tobita, M., Imakiire, T., & Ozawa, S (2011), Interplate fault slip along the Japan  
564 Trench before the occurrence of the 2011 off the Pacific coast of Tohoku Earthquake as inferred  
565 from GPS data. *Earth, Planets and Space*, 63(7), 19. <https://doi.org/10.5047/eps.2011.06.053>
- 566 Sun, T., & Wang, K (2015), Viscoelastic relaxation following subduction earthquakes and its effects on  
567 afterslip determination. *J. Geophys. Res.*, 120(2), 1329–1344. <https://doi.org/10.1002/2014JB011707>
- 568 Takagi, R., Uchida, N., & Obara, K (2019), Along-Strike Variation and Migration of Long-Term Slow  
569 Slip Events in the Western Nankai Subduction Zone, Japan. *J. Geophys. Res.*, 124(4), 3853–3880.  
570 <https://doi.org/10.1029/2018JB016738>
- 571 Takamatsu, N., Muramatsu, H., Abe, S., Hatanaka, Y., Furuya, T., Kakiage, Y., Ohashi, K., Kato, C.,  
572 Ohno, K., & Kawamoto, S. (2023), New GEONET analysis strategy at GSI: daily coordinates of  
573 over 1300 GNSS CORS in Japan throughout the last quarter century. *Earth, Planets and Space*,  
574 75(1), 49. <https://doi.org/10.1186/s40623-023-01787-7>
- 575 Tomita, F., Iinuma, T., Ohta, Y., Hino, R., Kido, M., & Uchida, N (2020), Improvement on spatial  
576 resolution of a coseismic slip distribution using postseismic geodetic data through a viscoelastic  
577 inversion. *Earth, Planets and Space*, 72(1), 84. <https://doi.org/10.1186/s40623-020-01207-0>
- 578 Tsang, L. L. H., Meltzner, A. J., Philiposian, B., Hill, E. M., Freymueller, J. T., & Sieh, K (2015), A 15  
579 year slow-slip event on the Sunda megathrust offshore Sumatra. *Geophys. Res. Lett.*, 42(16), 6630–  
580 6638. <https://doi.org/https://doi.org/10.1002/2015GL064928>
- 581 Uchida, N., Iinuma, T., Nadeau, R. M., Bürgmann, R., & Hino, R (2016), Periodic slowslip triggers  
582 megathrust zone earthquakes in northeastern Japan. *Science*, 351(6272), 488–492.  
583 <https://doi.org/10.1126/science.aad3108>
- 584 Villegas-Lanza, J. C., Nocquet, J.-M., Rolandone, F., Vallée, M., Tavera, H., Bondoux, F., Tran, T.,  
585 Martin, X., & Chlieh, M (2015), A mixed seismic–aseismic stress release episode in the Andean  
586 subduction zone. *Nat. Geosci.*, 9(2), 150–154. <https://doi.org/10.1038/ngeo2620>
- 587 Wessel, P., W. H. F. Smith, R. Scharroo, J. Luis, & F. Wobbe (2013), Generic Mapping Tools: Improved  
588 Version Released, *EOS Trans. AGU*, 94(45), 409–410. [doi:10.1002/2013EO450001](https://doi.org/10.1002/2013EO450001).

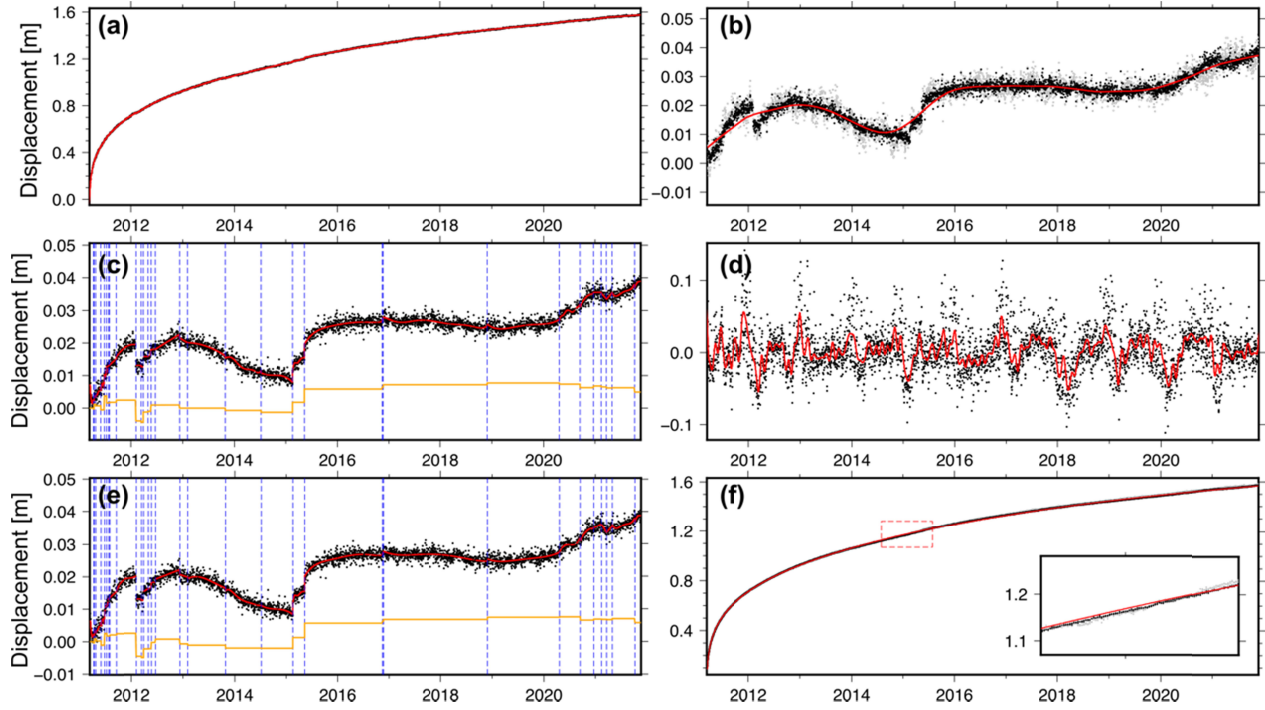
- 589 Widowski, S., Bock, Y., Zhang, J., Fang, P., & Genrich, J (1997), Southern California Permanent GPS  
590 Geodetic Array: Spatial filtering of daily positions for estimating coseismic and postseismic  
591 displacements induced by the 1992 Landers earthquake, *J. Geophys. Res.*, *102*(B8), 18057–18070.  
592 <https://doi.org/10.1029/97JB01378>
- 593 Yabuki, T., & Matsu'ura, M (1992), Geodetic data inversion using a Bayesian information criterion for  
594 spatial distribution of fault slip. *Geophys. J. Int.*, *109*(2), 363–375. [https://doi.org/10.1111/j.1365-  
595 246X.1992.tb00102.x](https://doi.org/10.1111/j.1365-246X.1992.tb00102.x)
- 596 Yamanaka, Y., & Kikuchi, M (2003), Source process of the recurrent Tokachi-oki earthquake on  
597 September 26, 2003, inferred from teleseismic body waves. *Earth, Planets and Space*, *55*, 21–24.  
598 <https://doi.org/10.1186/BF03352479>
- 599 Yamanaka, Y., & Kikuchi, M (2004), Asperity map along the subduction zone in northeastern Japan  
600 inferred from regional seismic data, *J. Geophys. Res.*, *109*, B07307.  
601 <https://doi.org/10.1029/2003JB002683>
- 602 Yokota, Y., & Koketsu, K (2015), A very long-term transient event preceding the 2011 Tohoku  
603 earthquake. *Nat. Comm.*, *6*, 5934. <https://doi.org/10.1038/ncomms6934>
- 604 Zhou, X., Cambiotti, G., Sun, W., & Sabadini, R (2014), The coseismic slip distribution of a shallow  
605 subduction fault constrained by prior information: the example of 2011 Tohoku (Mw 9.0)  
606 megathrust earthquake. *Geophys. J. Int.*, *199*, 981–995. <https://doi.org/10.1093/gji/ggu310>  
607
- 608



609

610 **Figure 1.** Black triangles show the GNSS sites used in this study. Gray circles show the 3d B-  
 611 spline nodes for Green's function library. Red and blue open stars show interplate and non-  
 612 interplate earthquakes with moment magnitudes of 6.7 and more, after the 2011 Tohoku  
 613 earthquake. Orange crosses indicate earthquakes with moment magnitudes between 6.5 and 6.7  
 614 after the 2011 Tohoku earthquake regardless of their mechanisms.

615

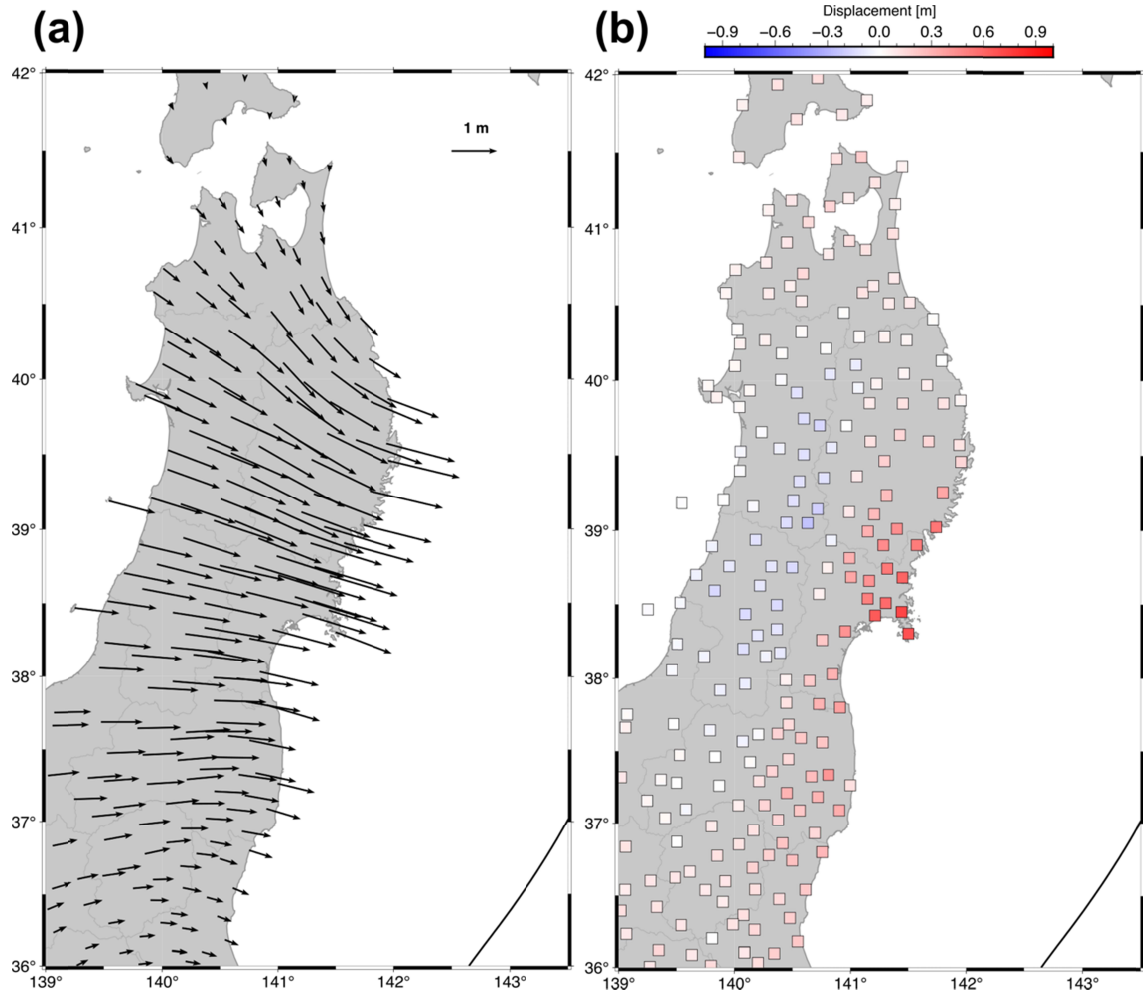


616

617 **Figure 2.** Example of GNSS pre-preprocessing in the EW component of the site 950167  
 618 (Yamada, Iwate Prefecture). The details of each panel are written in Section 2.1.

619

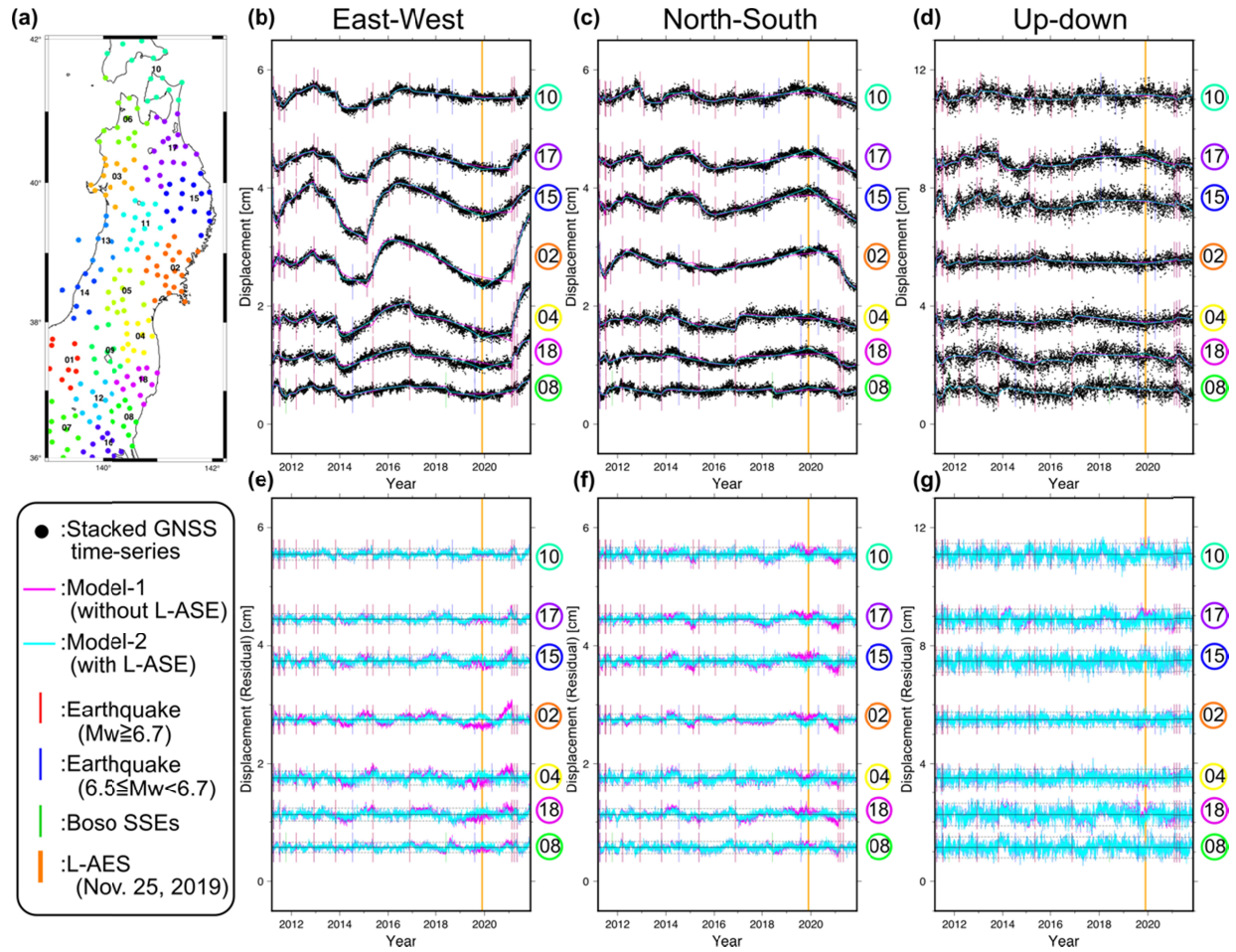
620



621

622 **Figure 3.** Cumulative post-seismic displacement associated with the 2011 Tohoku earthquake in  
 623 horizontal (a) and vertical (b) components. These displacements were calculated from Equation  
 624 (2) after the pre-processing.

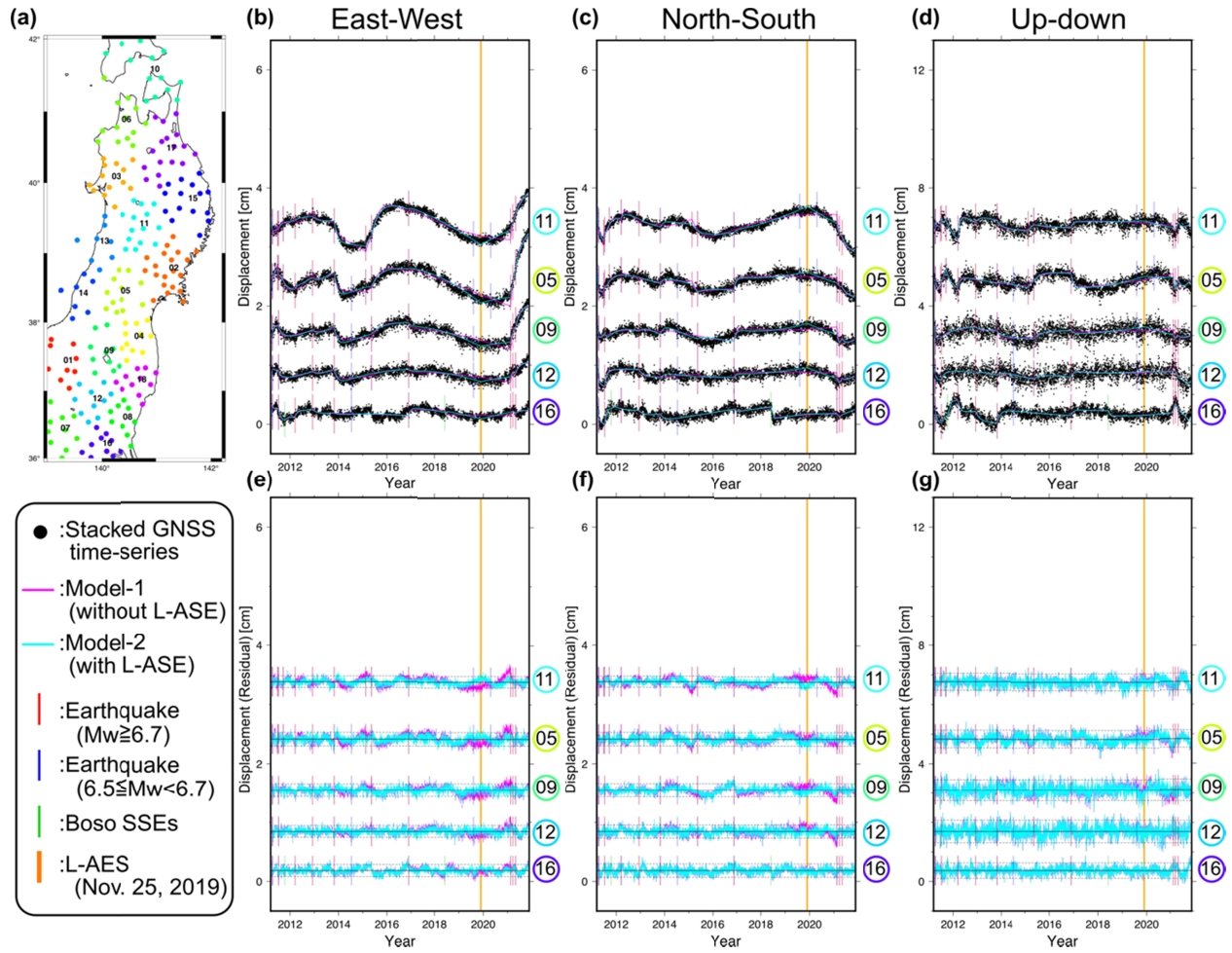
625



626

627 **Figure 4.** (a) GNSS site distribution. The colors indicate the site groups. (b–d) The stacked  
 628 GNSS time-series after pre-processing for the site groups near the eastern coastline in EW, NS,  
 629 and UD components. The magenta and cyan curves indicate the fitted curves of Model-1 and  
 630 Model-2, respectively. The vertical red, blue, green, and orange lines show the timings of near-  
 631 field earthquakes ( $M_w \geq 6.7$ ), near-field earthquakes ( $6.5 \leq M_w < 6.7$ ), the 2011 and 2018 Boso  
 632 SSEs, and the 2019 L-ASE, respectively. (e–g) The residual GNSS time-series of Model-1  
 633 (magenta) and Model-2 (cyan). The other symbols are same with (b–d).

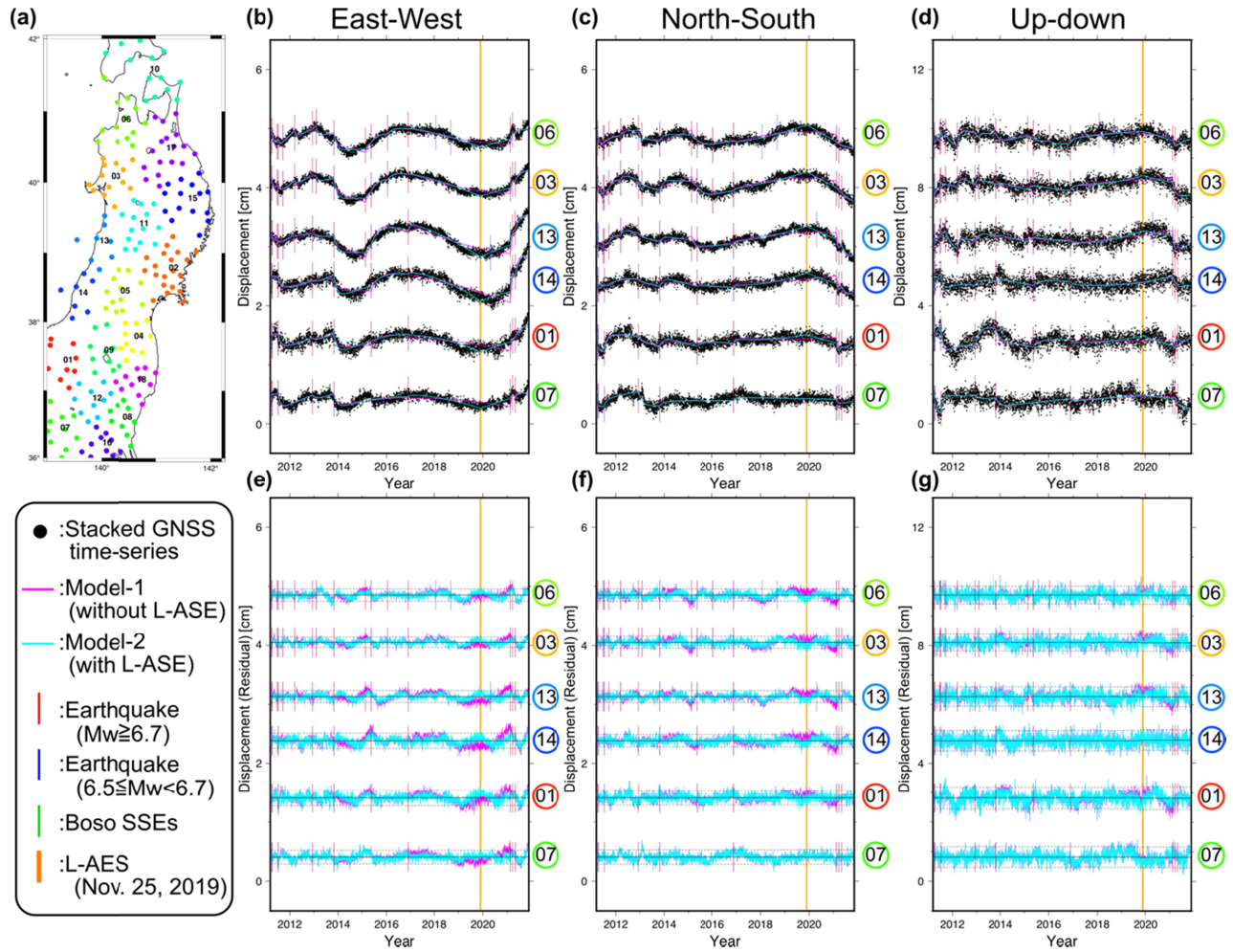
634



635

636 **Figure 5.** Stacked GNSS time-series for site groups in mid-Tohoku region. Symbols are shown  
 637 in the same manner as in Figure 4.

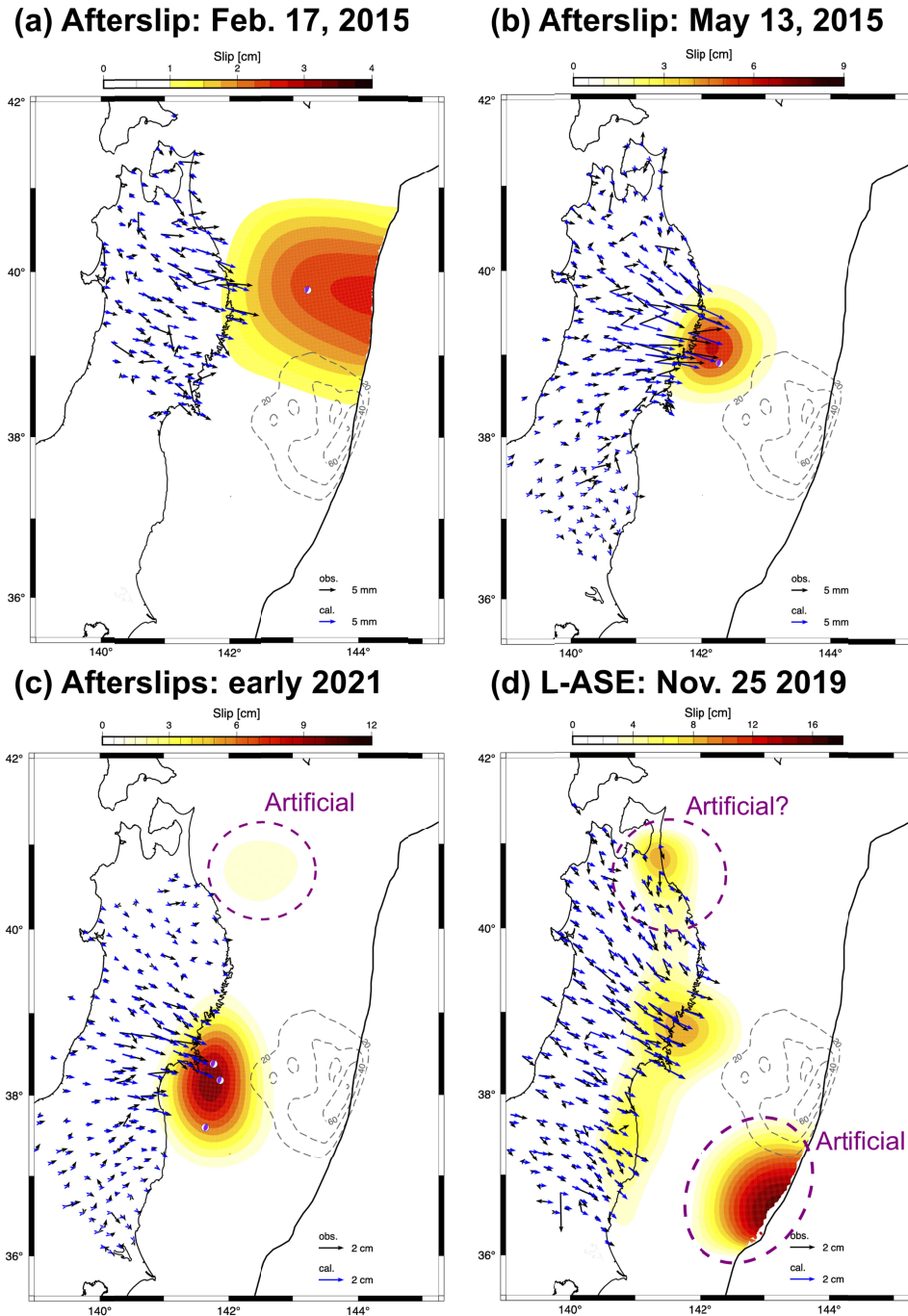
638



639

640 **Figure 6.** Stacked GNSS time-series for site groups along the western coastline. Symbols are  
 641 shown in the same manner as in Figure 4.

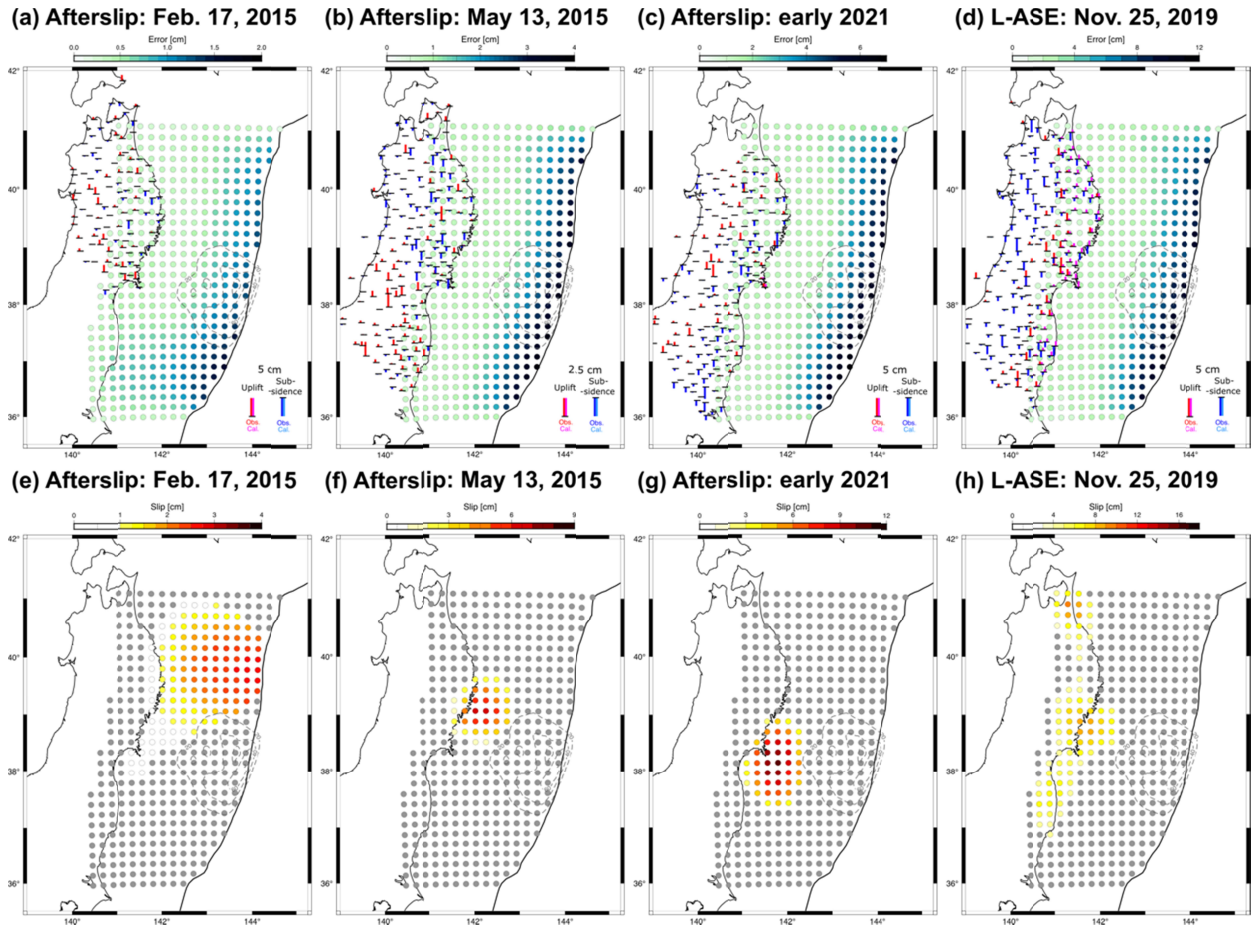
642



643

644 **Figure 7.** Color maps in (a)–(c) show the estimated afterslip distributions for the 2015 Feb. 17  
 645 Sanriku earthquake, the 2015 May 13 Miyagi earthquake, and the 2021 Mar. 20 and May 1  
 646 Miyagi earthquakes, respectively. The color map in (d) shows the estimated aseismic slip  
 647 distribution of the 2019 L-ASE. The black and blue vectors show the observed and calculated  
 648 cumulative displacements, respectively (displacements due to the 2021 Feb. 13 Fukushima  
 649 earthquake are included in (c)). The mechanism solutions of the mainshocks are shown in (a)–  
 650 (c). Dotted contours show the coseismic slip distribution of the 2011 Tohoku earthquake (Iinuma  
 651 et al., 2012) with slip over 20 m.

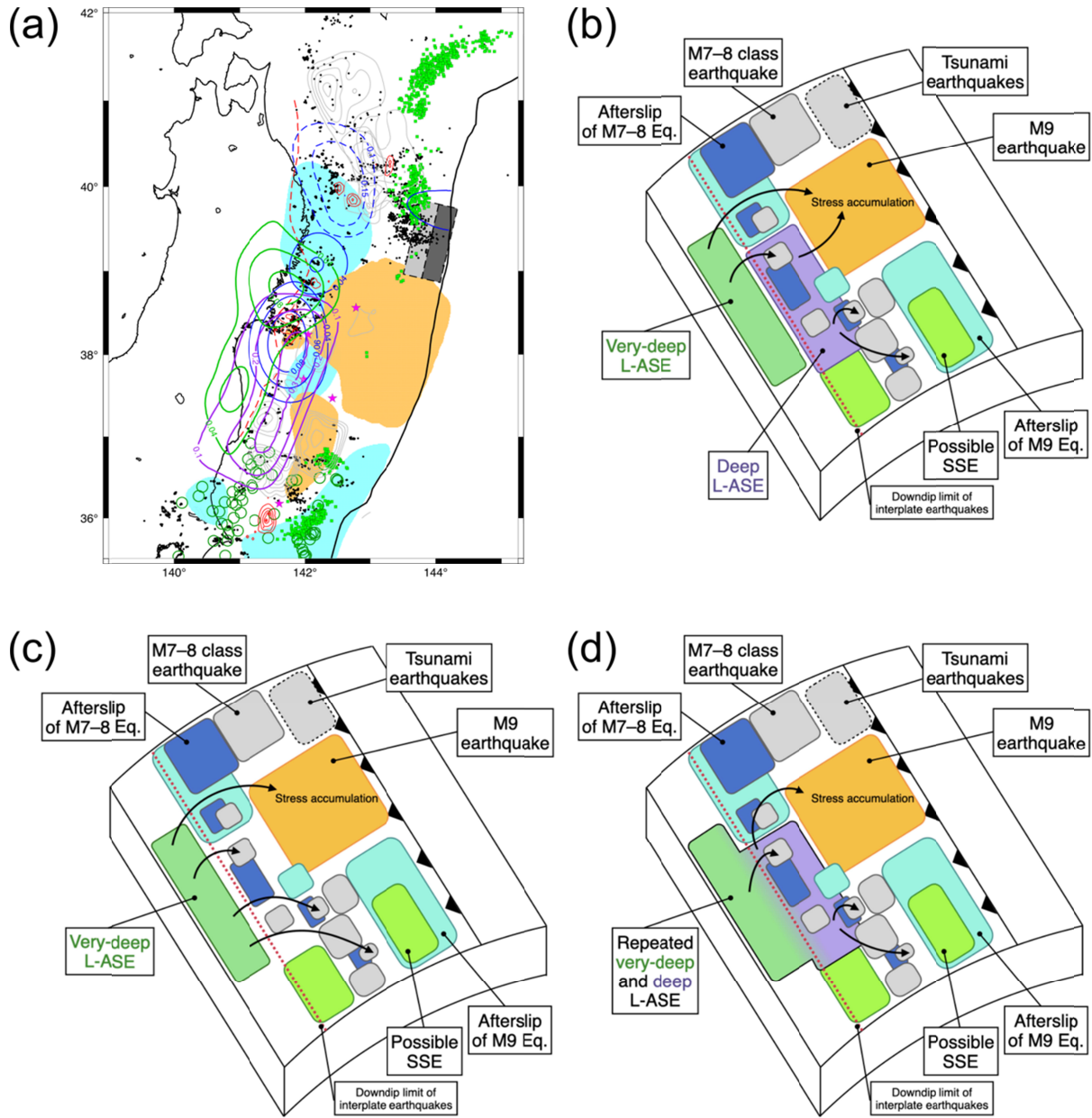
652



653

654 **Figure 8.** (a–d) Colored circles indicate the location of the 3d B-spline nodes of Green’s  
 655 function, and their colors indicate the estimation errors. The red and magenta vertical bars  
 656 represent the observed and calculated uplift displacements, respectively, and the blue and cyan  
 657 vertical bars represent the observed and calculated subsidence displacements, respectively. (e–h)  
 658 The gray circles demonstrate the inversion nodes with the slip below  $2\sigma$  estimation error, and the  
 659 other colored circles demonstrate the inversion nodes with the significant slip over  $2\sigma$  estimation  
 660 error. The dotted contours in all panels indicate the co-seismic slip distribution of the 2011  
 661 Tohoku earthquake (Inuma et al., 2012).

662



663

664 **Figure 9.** (a) Blue and green solid contours show the afterslip distributions and the 2019 L-ASE  
 665 of this study, respectively. Orange and cyan shaded areas show the coseismic and afterslip areas  
 666 of the 2011 Tohoku earthquake (Iinuma et al., 2012; Iinuma et al., 2016), respectively. Green  
 667 squares and black dots demonstrate the tremors (Nishikawa et al., 2019) and the interplate  
 668 earthquakes (Nakamura et al., 2016) after the 2011 Tohoku earthquake, respectively. Green open  
 669 circles show the possible SSEs (Nishimura, 2021). Dark and light gray rectangles show the major  
 670 tsunami sources of the 2011 Tohoku earthquake and the 1896 Meiji-Sanriku earthquake,  
 671 respectively (Satake et al., 2017). Gray and red contours show the M7 class earthquakes before  
 672 2002 (Nagai et al., 2001; Murotani et al., 2003; Yamanaka & Kikuchi, 2003; Yamanaka &  
 673 Kikuchi, 2004) and after 2011 Tohoku earthquakes (Japan Meteorological Agency solutions).  
 674 Magenta stars show epicenters of M7 class earthquakes after 2002 until the 2011 Tohoku  
 675 earthquake. Dotted blue and purple contours show afterslip of the 1994 Sanriku earthquake and

676 the 2002 L-ASE, respectively (Yokota & Koketsu, 2015). The red dotted curve indicates the  
677 downdip limit of the interplate earthquakes (Igarashi et al., 2001). (b–d) Schematic images of the  
678 possible scenarios associated with the L-ASEs.  
679